

A Bose-Einstein Condensate on a Synthetic Hall Cylinder

Chuan-Hsun Li,¹ Yangqian Yan,² Sayan Choudhury², David B. Blasing²,
Qi Zhou^{2,3,*}, Yong P. Chen^{2,1,3,†}

¹School of Electrical and Computer Engineering, Purdue University,
West Lafayette, Indiana 47907, USA

²Department of Physics and Astronomy, Purdue University, West Lafayette, Indiana 47907, USA

³Purdue Quantum Center, Purdue University, West Lafayette, Indiana 47907, USA

*To whom correspondence should be addressed; E-mail: zhou753@purdue.edu

†To whom correspondence should be addressed; E-mail: yongchen@purdue.edu

Abstract

Interplay between matter and fields in physical spaces with nontrivial geometries gives rise to many exotic quantum phenomena. However, their realizations are often impeded by experimental constraints. Here, we realize a Bose-Einstein condensate (BEC) on a synthetic cylindrical surface subject to a net radial synthetic magnetic flux, topologically equivalent to a two-dimensional (2D) Hall ribbon with two edges connected. This cylindrical surface comprises a real spatial dimension and a curved synthetic dimension formed by cyclically-coupled spin states. The BEC on such a Hall cylinder has counterintuitive properties unattainable by its counterparts in 2D planes. We observe Bloch oscillations of the BEC with doubled periodicity of the band structure, analogous to traveling on a Möbius strip, reflecting the BEC's emergent crystalline order with nonsymmorphic symmetry-protected band crossings. We further demonstrate such topological operations as gapping the band crossings and unzipping the cylinder. Our work opens the door to engineering synthetic curved spaces and observing intriguing quantum phenomena inherent to the topology of spaces.

Studies of matter and fields in spaces with nontrivial geometries play fundamentally important roles in many branches of physics such as general relativity and cosmology (1), photonics (2), and condensed matter physics (3). It is known that quantum systems in such spaces

often exhibit counterintuitive properties difficult to attain in flat spaces. Superfluids on a cylindrical surface as well as some other curved manifolds can carry vortices with no counterparts in 2D planes (4–6). Fractional quantum Hall states become degenerate on a torus, underlying the profound concept of topological order (7). Though novel quantum phenomena unique to spaces with non-trivial geometries have attracted longstanding theoretical interest since the birth of quantum mechanics, there have been limited experimental realizations due to technical challenges of fabricating such spaces and physical laws that further impose constraints. For instance, it is difficult to thread a net magnetic flux through the cylindrical surface of a nanotube. For a sphere and other closed surfaces, such a task is even impossible due to the absence of a magnetic monopole in nature.

The highly controllable laser-atom interactions have opened the possibility to bypass the constraints in conventional systems and deliver a variety of synthetic topological matters (8–11), such as artificial magnetic monopoles (12, 13), and bosonic (14–18) and fermionic (19–22) gases with synthetic spin-orbit coupling. Introducing the concept of “synthetic dimension”, for example using atoms’ internal degrees of freedom (23–25) or momentum states (26), has provided a new route to realizing high-dimensional systems and manipulating boundary conditions. So far, experimental studies have been focusing on spaces with relatively simple geometries, for instances, Hall ribbons with open boundary conditions (24, 25) equivalent to 2D systems whose edges are disconnected. In our experiments, we produce a 3D ^{87}Rb BEC with a typical atom number $\sim (1 - 2) \times 10^4$ in an optical dipole trap (17, 27). The BEC is then loaded to the cylindrical surface of a synthetic Hall cylinder by turning on a cyclic coupling among atomic (hyperfine) spin states, effectively delivering a periodic boundary condition in the synthetic dimension and connecting the two edges of a 2D Hall ribbon.

As shown in Fig. 1AB, four spin states, $|F, m_F\rangle = |2, 2\rangle, |2, 1\rangle, |1, 0\rangle, |1, 1\rangle$ relabeled as $|1\rangle, |2\rangle, |3\rangle, |4\rangle$, form discrete sites in the synthetic dimension (23) referred to as the w

direction. Utilizing $F = 1$ and $F = 2$ (hyperfine) manifolds makes a cyclic coupling in the w direction possible, since a transition of $\Delta m_F = \pm 2$ is extremely weak in the $F = 1$ manifold of alkali atoms (28). Counter-propagating Raman lasers along $\pm \hat{y}$, with an angular frequency difference $\Delta\omega_R$ and a coupling strength Ω , couple $|1\rangle$ and $|2\rangle$ as well as $|3\rangle$ and $|4\rangle$. The Raman lasers at the magic wavelength $\lambda \sim 790$ nm (29) set the photon recoil momentum $\hbar k_r = 2\pi\hbar/\lambda$ and recoil energy $E_r = \hbar^2 k_r^2 / (2m)$, where \hbar is the reduced Planck constant and m is the atomic mass of ^{87}Rb . Two microwave fields, with coupling strengths Ω_1 and Ω_2 , couple respectively $|2\rangle$ and $|3\rangle$, and $|1\rangle$ and $|4\rangle$. The combination of these Raman and microwave fields delivers a cyclic coupling, effectively a closed circle, in the w direction. Differently from other types of cyclic couplings previously studied for creating 2D spin-orbit couplings (21, 30) and Yang monopoles (13), our scheme synthesizes the y and the curved w dimensions into a “Hall” cylinder, a cylindrical surface with a net synthetic radial magnetic flux as schematized in Fig. 1C.

An atom obtains a net momentum of $\hbar K$ along $\pm \hat{y}$ from a Raman transition, thus acquiring a quantum mechanical y -dependent phase factor, $e^{\pm iKy}$ (31), where $K = 2k_r$. Such a phase has been used to engineer an artificial magnetic flux (23–25, 32, 33). Since the Raman-induced momentum transfer is along \hat{y} and the x and z -directions are decoupled from the cylindrical surface, the single-particle Hamiltonian describing the couplings in Fig. 1B and the atomic motions along \hat{y} can be written in the basis of $\{|1\rangle, |2\rangle, |3\rangle, |4\rangle\}$ as (31)

$$H = \frac{\hat{p}_y^2}{2m} \mathbf{I} + \begin{pmatrix} -\delta_R & \frac{\Omega}{2} e^{iKy} & 0 & \frac{\Omega_2}{2} \\ \frac{\Omega^*}{2} e^{-iKy} & \varepsilon_0 & \frac{\Omega_1}{2} & 0 \\ 0 & \frac{\Omega_1^*}{2} & \varepsilon_0 & \frac{\Omega}{2} e^{iKy} \\ \frac{\Omega_2^*}{2} & 0 & \frac{\Omega^*}{2} e^{-iKy} & \delta_R \end{pmatrix}, \quad (1)$$

where $\hat{p}_y = -i\hbar \frac{\partial}{\partial y}$ is the momentum operator along \hat{y} , \mathbf{I} is the identity matrix, the detuning δ_R is zero in this work, ε_0 is the quadratic Zeeman shift. H has four unique features. First, the Raman-induced y -dependent phase factor, e^{iKy} , cannot be gauged away due to the periodic

boundary condition implemented by the cyclic coupling, unlike open boundary conditions such as $\Omega_2 = 0$ (31). This makes H periodic in y , corresponding to an underlying real-space lattice with a period of $d = 2\pi/K$. Second, a total y -dependent phase factor e^{i2Ky} accumulated after an atom completes a cycle clockwise along \hat{w} (Fig. 1C) implies a net magnetic flux penetrating the cylindrical surface. An effective magnetic flux $\Phi/\Phi_0 = Kd/(2\pi) = 1$ piercing an area of $d \equiv 2\pi/K = \pi/k_r$ times one unit length along \hat{w} is indicated by a thick yellow arrow through shaded areas in Fig. 1C, where $\Phi_0 = 2\pi\hbar/e$ is the magnetic flux quantum and $q \equiv -e$ (e is the unit of electric charge) is defined as the effective charge of a particle. Third, a BEC on such a synthetic Hall cylinder described by H develops a crystalline order in its density along \hat{y} (Fig. 1C). As explained later, this density modulation has a period of $d/2$ (half period of the lattice and H) due to the underlying nonsymmorphic symmetry. We emphasize that unlike previous works using real-space external optical lattices (23–25), here the emergent crystalline order of atomic density is purely a result of “curving” a planar space to a cylinder. As shown later, the crystalline order vanishes on an “unzipped” cylinder when imposing an open boundary condition along \hat{w} , such as by turning off Ω_2 (even the effective magnetic flux remains the same, as represented by the same yellow arrows in Fig. 1C and Fig. 4A). Fourth, whereas the period of H is d , H is invariant under a translation of $d/2$ along \hat{y} followed by a unitary transformation along \hat{w} given by $|1\rangle \rightarrow |1\rangle$, $|2\rangle \rightarrow -|2\rangle$, $|3\rangle \rightarrow -|3\rangle$, $|4\rangle \rightarrow |4\rangle$. Such a nonsymmorphic symmetry (31) is of great interest because it can lead to symmetry-protected band crossings (10), which can play an important role in topological quantum matters such as topological semimetals (34). Because of the band crossings, unconventional Bloch oscillations in the momentum space that mimic the transport on a Möbius strip can arise (10, 35, 36).

The emergent lattice and BEC density modulation can also be understood in the momentum space. Fig. 2A illustrates laser and microwave induced couplings between the BEC wavefunction’s constituent plane waves, each characterized by a given spin state and mechanical

momentum along \hat{y} . Our cyclic coupling leads to two independent branches in the momentum-spin space, $H_1(q_y)$ and $H_2(q_y)$ represented by line-connected solid/dashed circles, where $\hbar q_y$ is the quasimomentum, $\hbar k_y = \hbar(q_y \pm nK)$ is the mechanical momentum, and n is an integer. On one hand, each branch satisfies $H_{i=1,2}(q_y) = H_{i=1,2}(q_y + n \times 2K)$, corresponding to a sublattice with a period of $2\pi/(2K) = d/2$ and thus the $d/2$ periodicity of the associated density modulation. On the other hand, these two branches are offset from each other by $\hbar K$. Thus, the energy spectrum $E(q_y)$ consists of two sets of bands, $E_1(q_y)$ and $E_2(q_y)$ that satisfy $E_1(q_y) = E_2(q_y + K)$. These two sets of bands intersect at the boundary of the Brillouin zone, $q_y = \pm\pi/d = \pm K/2$, when $E(q_y) = E(-q_y)$ is satisfied (31). Our calculations show that the phase of each spin state's wavefunction has a periodicity of either d or $d/2$ (31). As a specific example, we sketch in Fig. 1C the BEC wavefunction calculated at $q_y = 0$ (in the ground band shown in Fig. 2B), showing the densities of different spin states. The $+$ and $-$ signs represent respectively a phase 0 and π at the positions of maximum density. Therefore, the phase of the total wavefunction of the BEC has a periodicity of d , consistent with the size $(2\pi/d)$ of the Brillouin zone.

To probe the density's crystalline order with a nonsymmorphic symmetry, we perform spin-revolved quantum transport measurements, using Bloch oscillations of a BEC initially prepared (31) at $q_y = 0$ in either band 1 or band 2 in the first Brillouin zone (Fig. 2B). Subsequently, the dipole trap is abruptly turned off at $t_{hold} = 0$, allowing the atoms to fall under the gravity (towards $-\hat{y}$, Fig. 1A) for various time t_{hold} , during which the coupling fields remain at the final values. Such a procedure for quantum transport measurement, by turning off the trap abruptly while keeping the relevant coupling fields for various t_{hold} , is used for all experiments presented later. The force (F_g) due to gravity (with also a small contribution from other background fields in the experiment (31)) transports the BEC towards negative q_y , inducing Bloch oscillations in the periodic band structure. During Bloch oscillations, the total mechanical momentum along

\hat{y} of the BEC, $\hbar k_{\text{BEC}}$, directly probes the slope of the Bloch band (or the group velocity v_p) as a function of t_{hold} or q_y based on $\frac{\hbar k_{\text{BEC}}(q_y)}{m} = v_p(q_y) = \frac{1}{\hbar} \frac{dE(q_y)}{dq_y}$ (37), where E is the band (eigen)energy. Both v_p and E are functions of q_y , where $q_y = q_0 + F_g t_{\text{hold}}/\hbar$ is a function of t_{hold} , $F_g = d(\hbar q_y)/dt_{\text{hold}}$ is the total force measured in our experiments, and in our case the initial quasimomentum $\hbar q_0 = 0$. After various t_{hold} , we immediately turn off all the coupling fields to release the atoms for a 15-ms time-of-flight (TOF) including a 9-ms spin-resolved Stern-Gerlach process, and then perform absorption imaging. These TOF images reveal the spin and mechanical momentum compositions of a BEC at various t_{hold} and the corresponding q_y . We obtain $\hbar k_{\text{BEC}}$ by summing over population-weighted mechanical momentum components along \hat{y} (31). The q_y -dependent spin compositions of the BEC directly probe the spin texture of the Bloch band. The quasimomentum of the BEC at t_{hold} can be measured (31) by the displacement of the mechanical momentum components of, say $|1\rangle$ and $|4\rangle$, at t_{hold} relative to their mechanical momentum components at $t_{\text{hold}} = 0$ ($q_y = 0$).

TOF images obtained for the initial preparations in either band 1 or band 2 are shown respectively in Fig. 2C and Fig. 2D, with their corresponding analyzed data (dots in Fig. 2E-H) labeled by either band 1 or band 2. The total mechanical momentum ($\hbar k_{\text{BEC}}$) versus t_{hold} and versus quasimomentum are respectively shown in Fig. 2E and Fig. 2F. The fractional spin populations in states $|1\rangle$ and $|4\rangle$, and in states $|2\rangle$ and $|3\rangle$, versus t_{hold} are shown in Fig. 2GH. Two notable features are revealed. First, we observe in Fig. 2CD that spin and momentum compositions of the BEC repeatedly show up with a period of $2\hbar K$ in quasimomentum (or a period of ~ 2.6 ms in time), twice the $\hbar K$ periodicity of the band structure (Fig. 2B). Such a double periodicity is also observed in Fig. 2F, which demonstrates the $2\hbar K$ periodicity of Bloch oscillations in quasimomentum. This transport behavior is analogous to traveling on a Möbius strip: atoms have to travel twice the period of the band structure to reach the same quantum state (up to a phase). According to the momentum-position duality, the observed $2\hbar K$ periodicity

(twice the period of the band structure) of Bloch oscillations is consistent with the calculated $d/2$ periodicity (half the period of the lattice described by H) of the real-space densities illustrated in Fig. 1C. Note that the q_y in Fig. 2F is plotted modulo $2K$ (i.e., q_y is equivalent to $q_y \pm n \times 2K$), only between $-K$ and K for both band 1 and band 2 due to their $2K$ periodicity in q_y . This $2\hbar K$ periodicity is also reflected by the observation of the $2\hbar K$ separation between different mechanical momentum components for each spin state in Fig. 2CD. Second, we observe that the spin and mechanical momentum composition of the BEC at a given t_{hold} or q_y in Fig. 2C are consistent with those in Fig. 2D with an offset by ~ 1.3 ms or $\sim K$. Such an offset in t_{hold} or q_y is also respectively observed in Fig. 2EGH and Fig. 2F, where data of band 1 and band 2 exhibit out-of-phase Bloch oscillations in t_{hold} or q_y . These observed out-of-phase Bloch oscillations with a double period of the band structure is consistent with the feature of band crossings: atoms traveling to the band touching points would undergo a perfect (adiabatic) transition from the ground band to the first excited band because of the vanishing band gap (38), unlike conventional Landau-Zener tunnelings with a finite band gap (17).

Therefore, during Bloch oscillations, if we regard the trajectory of the BEC in the momentum space as one band, band 1 and band 2 between $q_y = -1.5K$ ($1.5K$) and $-0.5K$ ($0.5K$) become respectively the first excited and the ground bands as labeled in Fig. 2B. Consequently, both bands have a periodicity of $2\hbar K$, doubling the reciprocal lattice vector $\hbar K$, and are exactly the same but shifted from each other by $\hbar K$, thus giving rise to band crossings occurring with a period of $\hbar K$. The presence of band crossings is another manifestation of the nonsymmorphic symmetry discussed above. Further, since Bloch oscillations can be used to map out (39) the band structure, Fig. 2F can directly reveal the lowest two crossing bands in Fig. 2B. In Fig. 2E-H, the experimental data are in agreement with theoretical calculations (solid lines) (31) using the same parameters as used in Fig. 2B and the average of the measured $d(\hbar q_y)/d(t_{hold}) = F_g$ (31).

These nonsymmorphic symmetry-protected band crossings remain under any perturbations respecting the symmetry, such as variations of parameters in Equation (1). Thus, the demonstrated “momentum-space Möbius strip” is also protected by the nonsymmorphic symmetry. It is then interesting to introduce perturbations that break the nonsymmorphic symmetry and probe the resulting changes in the band structure by Bloch oscillations. As shown in Fig. 3A, the nonsymmorphic symmetry can be broken by applying a radio frequency (RF) wave (with an angular frequency set to be the same as the Raman lasers’ angular frequency difference $\Delta\omega_R$) to couple $|1\rangle$ and $|2\rangle$ as well as $|3\rangle$ and $|4\rangle$, in addition to the Raman and microwave couplings. This results in a new Hamiltonian, H' (31), which adds constant RF coupling terms to the entries corresponding to Raman couplings in the matrix in Equation (1) and therefore is no longer invariant under the nonsymmorphic symmetry. Nevertheless, both H and H' still have the same periodicity of $d = 2\pi/K$ in the real space and the corresponding band structures have the same periodicity $\hbar K$ in the momentum space. However, the two branches (each has a period of $2\hbar K$) in Fig. 2A merge into one that has a period of $\hbar K$, giving rise to a new band structure (Fig. 3C) that has band gap opening at the crossing points observed in Fig. 2B. We probe this new periodic band structure by performing the quantum transport measurement using the same procedure as before. Fig. 3D presents TOF images at various t_{hold} and the corresponding q_y , with the analyzed data (dots) for the total mechanical momentum versus t_{hold} and quasimomentum respectively shown in Fig. 3EF. As shown in Fig. 3D-F, the oscillations of BEC’s spin and mechanical momentum composition and the total momentum have a period of ~ 1.3 ms or $\hbar K$, half the period as those observed in Fig. 2. The $\hbar K$ periodicity is now identical to the period of the lattice and H' , suggesting that q_y becomes equivalent to $q_y \pm nK$. This $\hbar K$ periodicity is also reflected by the observation of the $\hbar K$ separation between different mechanical momentum components for each spin state in Fig. 3D. Based on the observed dynamics, the symmetry-breaking perturbation has opened gaps at the crossing points in the band structure

and effectively performed a topology-change operation of “untwisting” the Möbius strip in the momentum space.

Lastly, we demonstrate another topological operation, by “unzipping” the cyclic coupling thus turning the cylindrical surface into a planar 2D ribbon, where the emergent lattice, BEC density modulation, and Bloch oscillations disappear. Theoretically, this is because when removing one segment of the cyclic coupling and effectively imposing an open boundary condition in the w direction, for instance, by setting $\Omega_2 = 0$ (Fig. 4A), the Raman-imprinted phase factor e^{iKy} in Equation (1) can be gauged away (31). In our experiments, we keep couplings Ω and Ω_1 but remove Ω_2 in Fig. 1B, using the same parameters as used in Fig. 2B except $\Omega_2 = 0$. This results in a single-particle dispersion shown in Fig. 4B, which we probe by performing the similar quantum transport measurement for a BEC initially prepared at the minimum of the right well ($q_y \approx K$). Fig. 4C presents TOF images at various t_{hold} and the corresponding q_y , with analyzed data (dots) for the total mechanical momentum versus t_{hold} shown in Fig. 4D and fractional spin populations versus t_{hold} shown in Fig. 4E. Data in Fig. 4C-E do not exhibit a periodicity, consistent with the observation of only one mechanical momentum component for each spin state in TOF images. These observations are consistent with the theoretical calculations (solid lines in Fig. 4DE) using the same parameters as used in Fig. 4B. Because the dispersion relation is not a periodic band structure like those in Fig. 2B and Fig. 3C, $\hbar k_{BEC}$ eventually keeps increasing due to the gravity. The spin composition of the BEC is initially dominated by $|4\rangle$ but becomes dominated by $|1\rangle$ at later times, consistent with the calculated spin texture of the dispersion relation.

Synthetic spaces are highly controllable and able to lift many constraints in real physical spaces. A BEC on a synthetic Hall cylinder has allowed us to access quantum phenomena absent in planar 2D spaces. Manipulations of couplings between spin states constituting the synthetic dimension have allowed us to perform such topological operations as gapping the

band crossings and “unzipping” the cylinder. Our work paves the way for future theoretical and experimental efforts of engineering the geometry and topology of a broader range of synthetic spaces, including curved spaces, to explore unprecedented quantum phenomena.

References and Notes

1. S. M. Carroll, *Spacetime and geometry: An introduction to general relativity* (Addison-Wesley, 2004).
2. N. Schine, A. Ryou, A. Gromov, A. Sommer, J. Simon, *Nature* **534**, 671 (2016).
3. H. Kleinert, *Gauge Fields in Condensed Matter* (World Scientific, 1989).
4. A. M. Turner, V. Vitelli, D. R. Nelson, *Rev. Mod. Phys.* **82**, 1301 (2010).
5. T.-L. Ho, B. Huang, *Phys. Rev. Lett.* **115**, 155304 (2015).
6. N.-E. Guenther, P. Massignan, A. L. Fetter, *Phys. Rev. A* **96**, 063608 (2017).
7. X. G. Wen, Q. Niu, *Phys. Rev. B* **41**, 9377 (1990).
8. J. Dalibard, F. Gerbier, G. Juzeliūnas, P. Öhberg, *Rev. Mod. Phys.* **83**, 1523 (2011).
9. N. Goldman, J. C. Budich, P. Zoller, *Nature Physics* **12**, 639 (2016).
10. S.-L. Zhang, Q. Zhou, *Journal of Physics B: Atomic, Molecular and Optical Physics* **50**, 222001 (2017).
11. O. Boada, A. Celi, J. Rodriguez-Laguna, J. I. Latorre, M. Lewenstein, *New Journal of Physics* **17**, 045007 (2015).
12. M. W. Ray, E. Ruokokoski, S. Kandel, M. Möttönen, D. S. Hall, *Nature* **505**, 657 (2014).

13. S. Sugawa, F. Salces-Carcoba, A. R. Perry, Y. Yue, I. B. Spielman, *Science* **360**, 1429 (2018).
14. Y.-J. Lin, K. Jiménez-García, I. B. Spielman, *Nature* **471**, 83 (2011).
15. J.-Y. Zhang, *et al.*, *Phys. Rev. Lett.* **109**, 115301 (2012).
16. C. Qu, C. Hamner, M. Gong, C. Zhang, P. Engels, *Phys. Rev. A* **88**, 021604 (2013).
17. A. J. Olson, *et al.*, *Phys. Rev. A* **90**, 013616 (2014).
18. Z. Wu, *et al.*, *Science* **354**, 83 (2016).
19. P. Wang, *et al.*, *Phys. Rev. Lett.* **109**, 095301 (2012).
20. L. W. Cheuk, *et al.*, *Phys. Rev. Lett.* **109**, 095302 (2012).
21. L. Huang, *et al.*, *Nature Physics* **12**, 540 (2016).
22. S. Kolkowitz, *et al.*, *Nature* **542**, 66 (2017).
23. A. Celi, *et al.*, *Phys. Rev. Lett.* **112**, 043001 (2014).
24. B. K. Stuhl, H.-I. Lu, L. M. Aycock, D. Genkina, I. B. Spielman, *Science* **349**, 1514 (2015).
25. M. Mancini, *et al.*, *Science* **349**, 1510 (2015).
26. B. Gadway, *Phys. Rev. A* **92**, 043606 (2015).
27. A. J. Olson, R. J. Niffenegger, Y. P. Chen, *Phys. Rev. A* **87**, 053613 (2013).
28. I. H. Deutsch, P. S. Jessen, *Optics Communications* **283**, 681 (2010).
29. L. J. LeBlanc, J. H. Thywissen, *Phys. Rev. A* **75**, 053612 (2007).

- 30. D. L. Campbell, G. Juzeliūnas, I. B. Spielman, *Phys. Rev. A* **84**, 025602 (2011).
- 31. Materials and methods are available as supplementary materials.
- 32. H. Miyake, G. A. Siviloglou, C. J. Kennedy, W. C. Burton, W. Ketterle, *Phys. Rev. Lett.* **111**, 185302 (2013).
- 33. M. Aidelsburger, *et al.*, *Phys. Rev. Lett.* **111**, 185301 (2013).
- 34. A. A. Burkov, *Nature Materials* **15**, 1145 (2016).
- 35. K. Shiozaki, M. Sato, K. Gomi, *Phys. Rev. B* **91**, 155120 (2015).
- 36. Q.-Z. Wang, C.-X. Liu, *Phys. Rev. B* **93**, 020505 (2016).
- 37. M. Ben Dahan, E. Peik, J. Reichel, Y. Castin, C. Salomon, *Phys. Rev. Lett.* **76**, 4508 (1996).
- 38. S.-L. Zhang, Q. Zhou, *Phys. Rev. A* **95**, 061601 (2017).
- 39. E. Peik, M. Ben Dahan, I. Bouchoule, Y. Castin, C. Salomon, *Phys. Rev. A* **55**, 2989 (1997).

Acknowledgements

Our experiment has been supported by NSF grant PHY-1708134. D. B. B. also acknowledges support by the Purdue Research Foundation Ph.D. fellowship. Q. Z. acknowledges startup funds from Purdue.

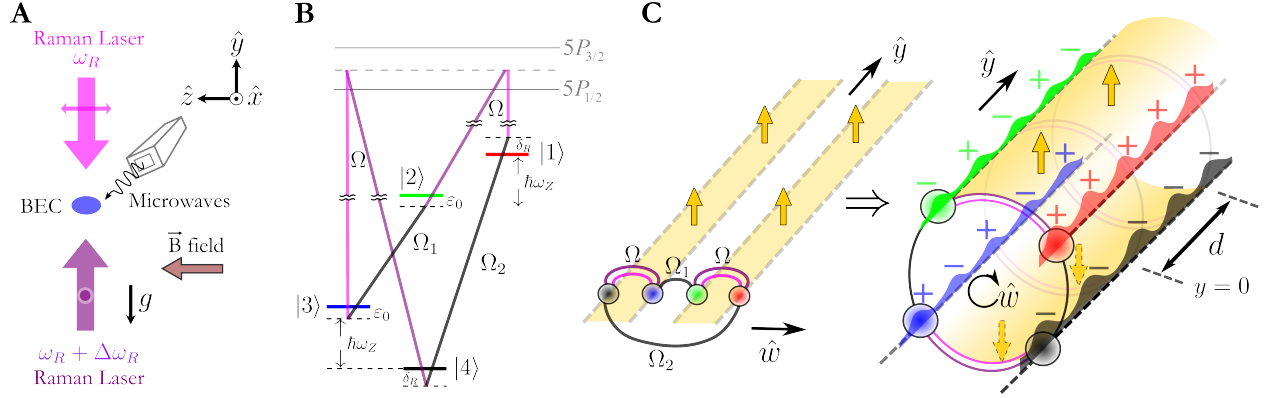


Figure 1: Experimental setup for realizing a synthetic Hall cylinder. (A-B) Raman lasers with orthogonal linear polarizations (A, double-headed arrows) counter-propagate along \hat{y} . Gravity “ g ” is towards $-\hat{y}$. Hyperfine spin states (B, indicated by different colors) $|1\rangle$ and $|2\rangle$, and $|3\rangle$ and $|4\rangle$ are Raman coupled with strength Ω . Linear Zeeman splitting $\hbar\omega_Z \approx \hbar\Delta\omega_R \approx h \times (3.5 \text{ MHz})$ is generated by a bias magnetic field $\vec{B} = B\hat{z}$, which sets the detuning $\delta_R = \hbar(\Delta\omega_R - \omega_Z)$ to be zero in our experiments. The quadratic Zeeman shift $\varepsilon_0 \approx 2.4 E_r$. Microwaves (frequency $\approx 6.8 \text{ GHz}$, from a microwave horn) propagating in the $x - y$ plane couple $|2\rangle$ and $|3\rangle$, and $|1\rangle$ and $|4\rangle$, with respective strengths $\Omega_{1,2}$. Four spin states as discrete sites are cyclically-coupled (a periodic boundary condition) to form a closed circle in the synthetic dimension \hat{w} . (C) A Hall ribbon (left) in the 2D plane with two connected edges along \hat{w} is topologically equivalent to a cylindrical surface (right) subject to a radial magnetic flux (thick yellow arrows) generated by the Raman coupling. The emergent crystalline order of the BEC density has a periodicity of $d/2$, half period (d) of the lattice and the Hamiltonian H . For a BEC at $q_y = 0$ in the ground band of Fig. 2B, the wavefunction’s phase (indicated by $+$ and $-$) of each spin component has a periodicity of either d or $d/2$, leading to a d periodicity in the BEC wavefunction.

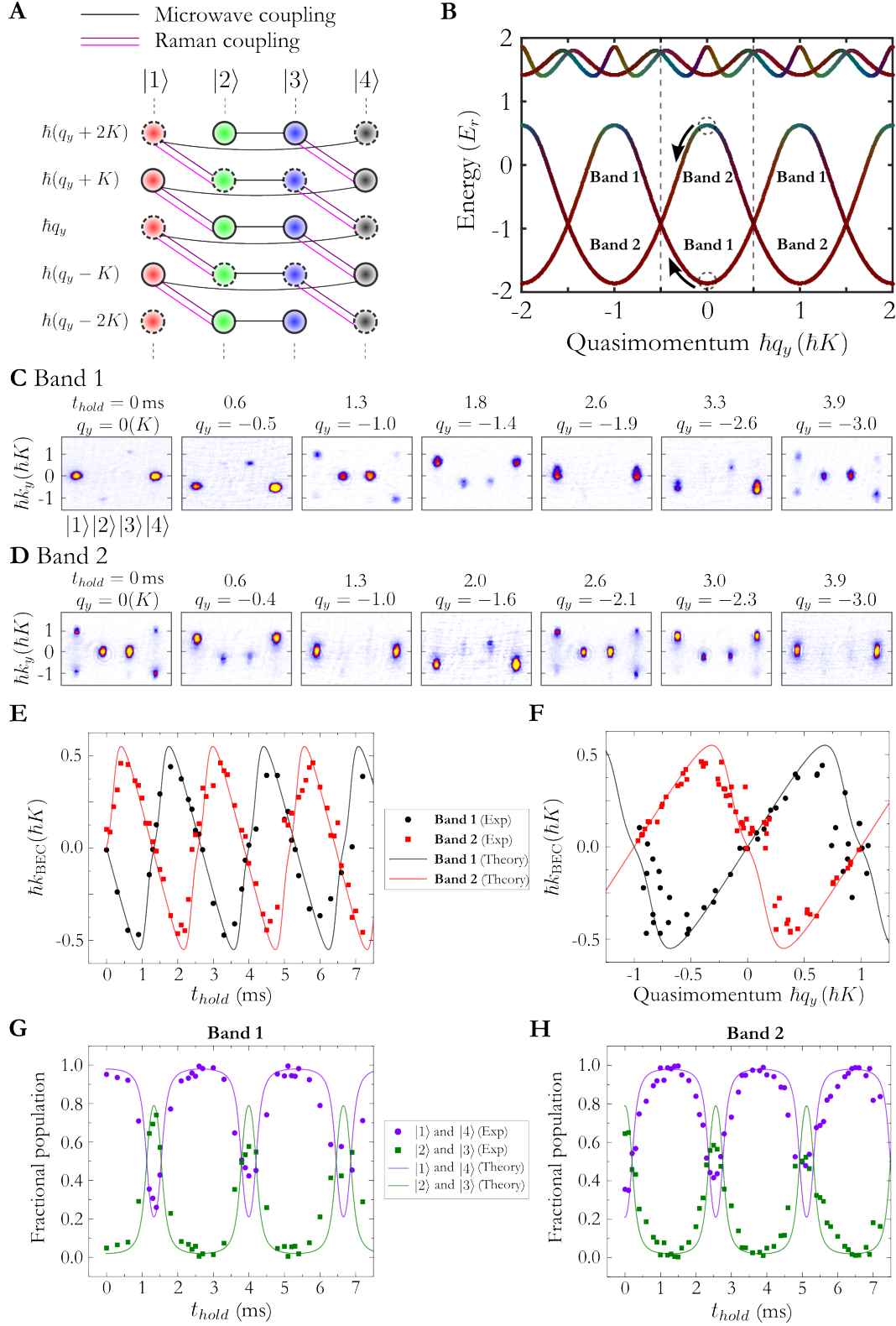


Figure 2: Band structure with a nonsymmorphic symmetry and observed Bloch oscillations. (A) Laser and microwave induced couplings between spin and mechanical momentum states. The cyclic coupling leads to an infinite number of mechanical momentum components $\hbar(q_y \pm nK)$ along \hat{y} . The underlying nonsymmorphic symmetry is manifested in the two independent branches (marked by solid/dashed circles) offset from each other by $\hbar K = 2\hbar k_r$. (B) Calculated band structure using $\Omega = 2.3$, $\Omega_1 = 2.5$, $\Omega_2 = 3.4$, $\delta_R = 0$, and $\varepsilon_0 = 2.4$, all in units of E_r . The spin texture is revealed by colors determined by the population-weighted colors of the four spin states (31). The first Brillouin zone is between the dashed lines. The BEC initially prepared at $\hbar q_y = 0$ (dashed circles) in either band 1 or band 2 undergoes gravity-induced transport (indicated by arrows) and Bloch oscillations for various t_{hold} . (C-D) TOF images showing spin and mechanical momentum compositions of atoms taken at various t_{hold} and the corresponding q_y , respectively corresponding to the initial preparation in band 1 and band 2. Each TOF image (and the associated analyzed quantities presented later) is typically an average of a few repetitive measurements. (E-F) Total mechanical momentum of the BEC versus t_{hold} and quasimomentum, respectively. (G-H) Fractional spin populations versus t_{hold} .

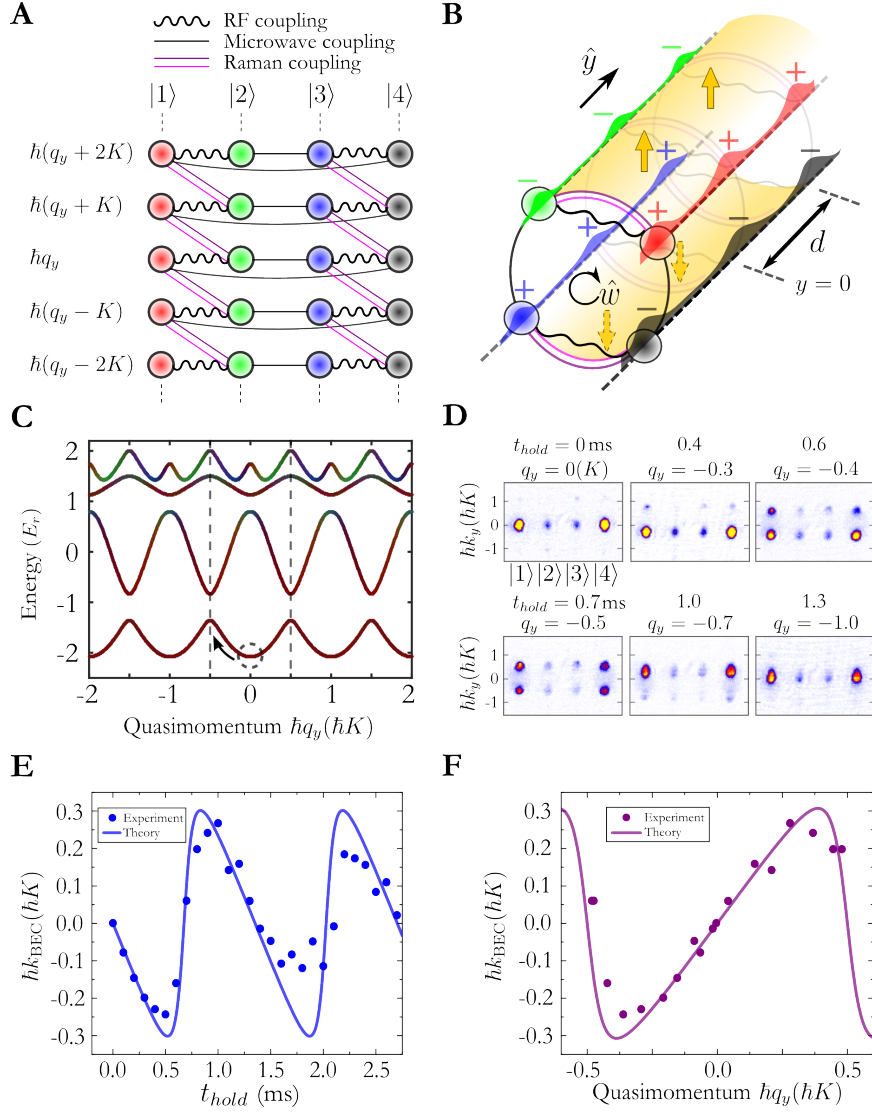


Figure 3: Breaking the nonsymmorphic symmetry and observed Bloch oscillations. (A) RF coupling (wiggling lines) merges the two independent branches in Fig. 2B, breaking the nonsymmorphic symmetry. (B) A cylinder with a broken nonsymmorphic symmetry, described by the Hamiltonian H' with lattice period d . For a BEC prepared at $q_y = 0$ in the ground band in (C), both the wavefunction's phase (indicated by + and -) and the crystalline order of the density have a periodicity of d , identical to the period of the lattice or the Hamiltonian H' . (C) Calculated band structure using the same parameters as used in Fig. 2B with the addition of $\Omega_{RF} = 1.6 E_r$. (D) TOF images at various t_{hold} for Bloch oscillations of a BEC starting from $q_y = 0$ (dashed circle in (C)). (E-F) Total mechanical momentum of the BEC versus t_{hold} and quasimomentum, respectively. The measured Bloch oscillations exhibit a periodicity of $\hbar K$ rather than the $2\hbar K$ observed in Fig. 2. Data in (F) correspond to the data in the first 1.5 ms in (E) before the Bloch oscillations exhibit notable damping.

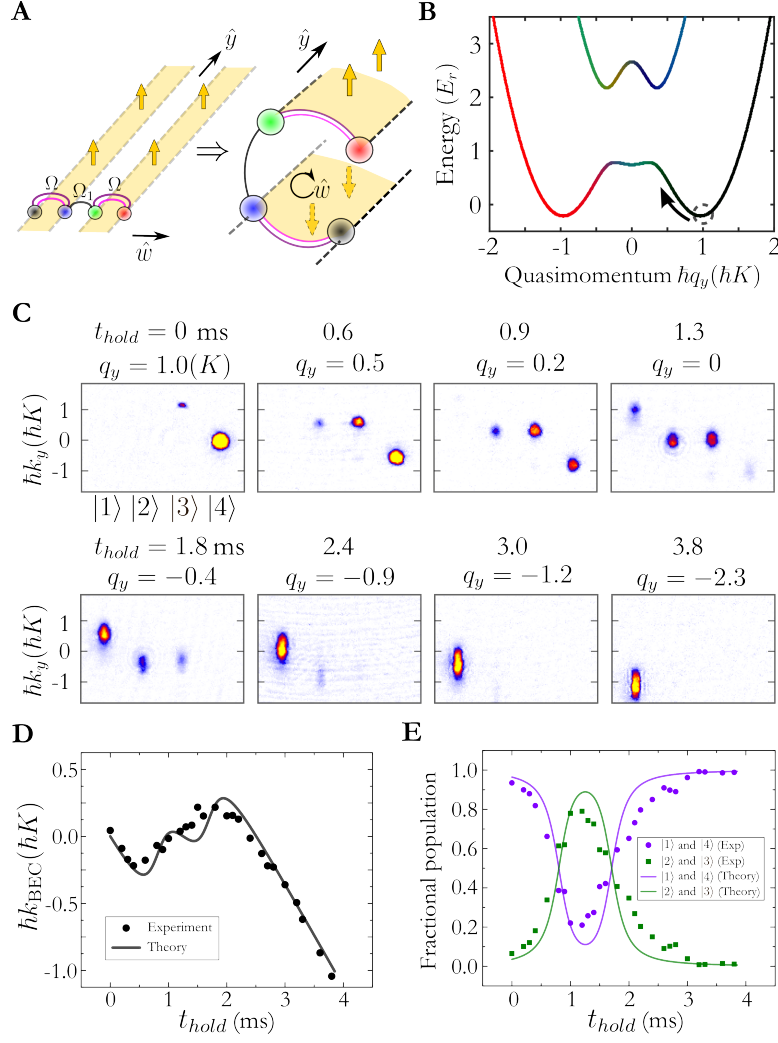


Figure 4: Unzipping the cylinder by breaking the cyclic coupling. (A) The unzipped Hall cylinder is topologically equivalent to a 2D planar Hall ribbon. (B) Dispersion relation calculated for $\Omega_2 = 0$, while keeping the other parameters the same as used in Fig. 2B. The BEC is initially prepared at the minimum of the right well ($q_y \approx K$, marked by the dashed circle). (C) TOF images at various t_{hold} and the corresponding quasimomentum for a BEC traveling towards negative q_y in the lowest band. (D) Total mechanical momentum of the BEC versus t_{hold} . (E) Fractional spin populations versus t_{hold} .

Supplementary Materials: a Bose-Einstein Condensate on a Synthetic Hall Cylinder

Single-particle Hamiltonians in the main text

We relabel the spin states $|2, 2\rangle = |\tilde{1}\rangle$, $|2, 1\rangle = |\tilde{2}\rangle$, $|1, 0\rangle = |\tilde{3}\rangle$, $|1, 1\rangle = |\tilde{4}\rangle$ (where tilde refers to a non-rotating frame, as explained below), with respective energies E_1 , E_2 , E_3 , and E_4 . Counter-propagating Raman lasers along $\pm\hat{y}$ with an angular frequency difference $\Delta\omega_R$ couple $|\tilde{1}\rangle$ and $|\tilde{2}\rangle$, and $|\tilde{3}\rangle$ and $|\tilde{4}\rangle$, with a coupling strength Ω . The wavelength (λ) of the Raman laser sets the recoil momentum $\hbar k_r$ and recoil energy $E_r = \hbar^2 k_r^2 / (2m)$, where $k_r = 2\pi/\lambda$ and $\lambda \sim 790$ nm. Two microwaves with angular frequencies ω_1 and ω_2 couple $|\tilde{2}\rangle$ and $|\tilde{3}\rangle$, and $|\tilde{1}\rangle$ and $|\tilde{4}\rangle$, with coupling strengths Ω_1 and Ω_2 , respectively. In Fig. 1B, we define $E_3 - E_4 = \hbar\omega_Z + \varepsilon_0$ and $E_1 - E_2 = \hbar\omega_Z - \varepsilon_0$, where $\hbar\omega_Z$ is the linear Zeeman splitting and ε_0 is the quadratic Zeeman shift. In our experiments, $\varepsilon_0 \sim 2.4 E_r$, given by the applied bias magnetic field (~ 5 gauss). The Raman laser detuning can be defined as $\delta_R = (2\hbar\Delta\omega_R - (E_3 - E_4) - (E_1 - E_2))/2 = \hbar(\Delta\omega_R - \omega_Z)$. The microwave detunings can be defined as $\delta_1 = \hbar\omega_1 - (E_2 - E_3)$ and $\delta_2 = \hbar\omega_2 - (E_1 - E_4)$.

In the following, we derive the single-particle Hamiltonians for various schemes of couplings in the main text. (1) For the cylindrical surface with a nonsymmorphic symmetry: the Hamiltonian H (used for Fig. 1C and relevant calculations shown below) and the corresponding momentum-space Hamiltonian H_{q_y} (used for Fig. 2). Both H and H_{q_y} take into account Ω and $\Omega_{1,2}$. (2) For the cylinder without a nonsymmorphic symmetry: the Hamiltonian H' and the corresponding momentum-space Hamiltonian H'_{q_y} (used for Fig. 3), taking into account Ω , $\Omega_{1,2}$, and Ω_{RF} . (3) For the unzipped cylinder: the momentum-space Hamiltonian H_{unzip} (used for Fig. 4), taking into account Ω and Ω_1 .

In this work, we focus on the atomic motion along \hat{y} . The free atomic Hamiltonian can be

written as:

$$\tilde{H}_{\text{free}} = \frac{\hat{p}_y^2}{2m} \mathbf{I} + E_1 |\tilde{1}\rangle \langle \tilde{1}| + E_2 |\tilde{2}\rangle \langle \tilde{2}| + E_3 |\tilde{3}\rangle \langle \tilde{3}| + E_4 |\tilde{4}\rangle \langle \tilde{4}|, \quad (\text{S2})$$

where \mathbf{I} is the identity matrix and $\hat{p}_y = -i\hbar \frac{\partial}{\partial y}$ is the momentum operator along \hat{y} . In the rotating wave approximation, the Hamiltonians describing the Raman and microwave couplings can be respectively written as (assuming the initial phases of these coupling fields are zero):

$$\tilde{H}_{\text{Raman}} = \frac{\Omega}{2} e^{i(Ky - \Delta\omega_R t)} (|\tilde{1}\rangle \langle \tilde{2}| + |\tilde{3}\rangle \langle \tilde{4}|) + h.c. \quad (\text{S3})$$

$$\tilde{H}_1 = \frac{\Omega_1}{2} e^{-i\omega_1 t} (|\tilde{2}\rangle \langle \tilde{3}|) + h.c. \quad (\text{S4})$$

$$\tilde{H}_2 = \frac{\Omega_2}{2} e^{-i\omega_2 t} (|\tilde{1}\rangle \langle \tilde{4}|) + h.c. \quad (\text{S5})$$

where $K = 2k_r$ and $h.c.$ stands for Hermitian conjugate. We can choose a rotating frame defined by the following unitary transformations to eliminate the time-dependent terms in Eqs. (S3-S5):

$$|\tilde{1}\rangle = e^{i\Delta\omega_R t} |1\rangle e^{i\frac{\omega_1}{2} t}, |\tilde{2}\rangle = e^{i\frac{\omega_1}{2} t} |2\rangle, |\tilde{3}\rangle = e^{-i\frac{\omega_1}{2} t} |3\rangle, |\tilde{4}\rangle = e^{-i\Delta\omega_R t} |4\rangle e^{-i\frac{\omega_1}{2} t}. \quad (\text{S6})$$

In such a rotating frame (without tilde),

$$\begin{aligned} H_{\text{free}} = & \frac{\hat{p}_y^2}{2m} \mathbf{I} + (E_1 - \hbar\Delta\omega_R - \frac{\hbar\omega_1}{2}) |1\rangle \langle 1| + (E_2 - \frac{\hbar\omega_1}{2}) |2\rangle \langle 2| \\ & + (E_3 + \frac{\hbar\omega_1}{2}) |3\rangle \langle 3| + (E_4 + \hbar\Delta\omega_R + \frac{\hbar\omega_1}{2}) |4\rangle \langle 4| \end{aligned} \quad (\text{S7})$$

$$H_{\text{Raman}} = \frac{\Omega}{2} e^{i(Ky)} (|1\rangle \langle 2| + |3\rangle \langle 4|) + h.c. \quad (\text{S8})$$

$$H_1 = \frac{\Omega_1}{2} (|2\rangle \langle 3|) + h.c. \quad (\text{S9})$$

$$H_2 = \frac{\Omega_2}{2} e^{-i\omega_2 t} e^{i2\Delta\omega_R t} e^{i\omega_1 t} (|1\rangle \langle 4|) + h.c. \quad (\text{S10})$$

where H_{Raman} and H_1 become time-independent. By further requiring

$$\omega_2 = 2\Delta\omega_R + \omega_1, \quad (\text{S11})$$

Eq. (S10) becomes $H_2 = \frac{\Omega_2}{2}(|1\rangle\langle 4|) + h.c.$, which is also time-independent. Eq. (S11) is called the resonance condition for the cyclic coupling. This resonance condition is realized in this work, depicted in Fig. 1B.

Therefore, in the rotating frame defined by Eq. (S6) and when the resonance condition in Eq. (S11) is fulfilled, $H = H_{\text{free}} + H_{\text{Raman}} + H_1 + H_2$ is time-independent and can be written in the basis of $\{|1\rangle, |2\rangle, |3\rangle, |4\rangle\}$ as:

$$H = \frac{\hat{p}_y^2}{2m}\mathbf{I} + \begin{pmatrix} E_1 - \hbar\Delta\omega_R - \frac{\hbar\omega_1}{2} & \frac{\Omega}{2}e^{i(Ky)} & 0 & \frac{\Omega_2}{2} \\ \frac{\Omega^*}{2}e^{-i(Ky)} & E_2 - \frac{\hbar\omega_1}{2} & \frac{\Omega_1}{2} & 0 \\ 0 & \frac{\Omega_1^*}{2} & E_3 + \frac{\hbar\omega_1}{2} & \frac{\Omega}{2}e^{i(Ky)} \\ \frac{\Omega_2^*}{2} & 0 & \frac{\Omega^*}{2}e^{-i(Ky)} & E_4 + \hbar\Delta\omega_R + \frac{\hbar\omega_1}{2} \end{pmatrix}. \quad (\text{S12})$$

From the above equation, we see that a Raman transition corresponds to a y -dependent phase factor, e^{iKy} , while a microwave transition does not lead to a position-dependent phase change. Referring to Fig. 1B, redefining all energies such that $E_3 + \hbar\omega_1/2 = \varepsilon_0$, using the definitions of ε_0 , δ_R , δ_1 , δ_2 , and the resonance condition Eq. (S11), we can obtain $\delta_1 + 2\delta_R = \delta_2$ and rewrite Eq. (S12) as

$$H = \frac{\hat{p}_y^2}{2m}\mathbf{I} + \begin{pmatrix} -\delta_R & \frac{\Omega}{2}e^{i(Ky)} & 0 & \frac{\Omega_2}{2} \\ \frac{\Omega^*}{2}e^{-i(Ky)} & \varepsilon_0 & \frac{\Omega_1}{2} & 0 \\ 0 & \frac{\Omega_1^*}{2} & \varepsilon_0 & \frac{\Omega}{2}e^{i(Ky)} \\ \frac{\Omega_2^*}{2} & 0 & \frac{\Omega^*}{2}e^{-i(Ky)} & \delta_R \end{pmatrix}. \quad (\text{S13})$$

Eq. (S13) is Eq. (1) in the main text. In this work, $\delta_R = \delta_1 = \delta_2 = 0$. To calculate the band structures, we derive the momentum-space Hamiltonian H_{q_y} by considering the coupling scheme in Fig. 2A. The spin and mechanical momentum states comprise a plane wave basis, denoted by

$$\{|\hbar(q_y + nK); m\rangle\} = \{e^{i(q_y + nK)y} |m\rangle\}, \quad (\text{S14})$$

where $\hbar(q_y + nK)$ is the mechanical momentum, $m = 1, 2, 3, 4$ labels the spin, $\hbar q_y$ is the quasimomentum, and n is an integer. Then, H_{q_y} can be written as:

$$H_{q_y} = \begin{pmatrix} \ddots & \vdots & \vdots & \vdots & \vdots & \vdots & \ddots \\ \dots & A_{-2} & B & 0 & 0 & 0 & \dots \\ \dots & B^\dagger & A_{-1} & B & 0 & 0 & \dots \\ \dots & 0 & B^\dagger & A_0 & B & 0 & \dots \\ \dots & 0 & 0 & B^\dagger & A_1 & B & \dots \\ \dots & 0 & 0 & 0 & B^\dagger & A_2 & \dots \\ \ddots & \vdots & \vdots & \vdots & \vdots & \vdots & \ddots \end{pmatrix}, \quad (\text{S15})$$

where A_n matrices are on the diagonal of H_{q_y} . Each A_n is a 4 by 4 matrix written in the basis of $\{|\hbar(q_y + nK); m\rangle\}$, where the four spin states have the same mechanical momentum (i.e., same n). Thus, A_n only includes microwave couplings. At $\delta_R = 0$, we obtain

$$A_n = \begin{pmatrix} \frac{\hbar^2}{2m}(q_y + nK)^2 & 0 & 0 & \frac{\Omega_2}{2} \\ 0 & \frac{\hbar^2}{2m}(q_y + nK)^2 + \varepsilon_0 & \frac{\Omega_1}{2} & 0 \\ 0 & \frac{\Omega_1^*}{2} & \frac{\hbar^2}{2m}(q_y + nK)^2 + \varepsilon_0 & 0 \\ \frac{\Omega_2^*}{2} & 0 & 0 & \frac{\hbar^2}{2m}(q_y + nK)^2 \end{pmatrix}. \quad (\text{S16})$$

B is a 4 by 4 matrix accounting for the Raman coupling between adjacent A_n matrices:

$$B = \begin{pmatrix} 0 & 0 & 0 & 0 \\ \Omega/2 & 0 & 0 & 0 \\ 0 & 0 & 0 & 0 \\ 0 & 0 & \Omega/2 & 0 \end{pmatrix}. \quad (\text{S17})$$

H' can be obtained by adding the RF coupling Ω_{RF} to H . Since Ω_{RF} couples $|1\rangle$ and $|2\rangle$, and $|3\rangle$ and $|4\rangle$, we obtain

$$H' = \frac{\hat{p}_y^2}{2m} \mathbf{I} + \begin{pmatrix} -\delta_R & \frac{\Omega_{RF}}{2} + \frac{\Omega}{2} e^{i(Ky)} & 0 & \frac{\Omega_2}{2} \\ \frac{\Omega_{RF}^*}{2} + \frac{\Omega^*}{2} e^{-i(Ky)} & \varepsilon_0 & \frac{\Omega_1}{2} & 0 \\ 0 & \frac{\Omega_1^*}{2} & \varepsilon_0 & \frac{\Omega_{RF}}{2} + \frac{\Omega}{2} e^{i(Ky)} \\ \frac{\Omega_2^*}{2} & 0 & \frac{\Omega_{RF}^*}{2} + \frac{\Omega^*}{2} e^{-i(Ky)} & \delta_R \end{pmatrix}. \quad (\text{S18})$$

Since RF waves only couple spin states that have the same mechanical momentum, H'_{q_y} would

have the same form as Eq. (S15) but with a modified A_n denoted by A'_n :

$$A'_n = \begin{pmatrix} \frac{\hbar^2}{2m}(q+nK)^2 & \frac{\Omega_{RF}}{2} & 0 & \frac{\Omega_2}{2} \\ \frac{\Omega_{RF}^*}{2} & \frac{\hbar^2}{2m}(q+nK)^2 + \varepsilon_0 & \frac{\Omega_1}{2} & 0 \\ 0 & \frac{\Omega_1^*}{2} & \frac{\hbar^2}{2m}(q+nK)^2 + \varepsilon_0 & \frac{\Omega_{RF}}{2} \\ \frac{\Omega_2^*}{2} & 0 & \frac{\Omega_{RF}^*}{2} & \frac{\hbar^2}{2m}(q+nK)^2 \end{pmatrix}. \quad (\text{S19})$$

For H_{unzip} , only Ω and Ω_1 are present. We can apply a unitary transformation

$$\hat{U}_0 = \begin{pmatrix} e^{-iKy} & 0 & 0 & 0 \\ 0 & 1 & 0 & 0 \\ 0 & 0 & 1 & 0 \\ 0 & 0 & 0 & e^{iKy} \end{pmatrix} \quad (\text{S20})$$

to H in Eq. (S13) (noting $\hat{p}_y^2/(2m)\mathbf{I} = \hbar^2 q_y^2/(2m)\mathbf{I}$ for plane wave basis) with $\Omega_2 = 0$ and $\delta_R = 0$, i.e., $\hat{U}_0 H \hat{U}_0^{-1}$, to gauge away the y -dependent phase factor and obtain H_{unzip} written in the basis of $\{|1\rangle, |2\rangle, |3\rangle, |4\rangle\}$ as:

$$H_{\text{unzip}} = \begin{pmatrix} \frac{\hbar^2}{2m}(q_y + K)^2 & \frac{\Omega}{2} & 0 & 0 \\ \frac{\Omega^*}{2} & \frac{\hbar^2}{2m}(q_y)^2 + \varepsilon_0 & \frac{\Omega_1}{2} & 0 \\ 0 & \frac{\Omega_1^*}{2} & \frac{\hbar^2}{2m}(q_y)^2 + \varepsilon_0 & \frac{\Omega}{2} \\ 0 & 0 & \frac{\Omega^*}{2} & \frac{\hbar^2}{2m}(q_y - K)^2 \end{pmatrix}. \quad (\text{S21})$$

If $\Omega_2 \neq 0$, the y -dependent phase factor cannot be gauged away because $\hat{U}_0 H \hat{U}_0^{-1}$ would still have the y -dependent terms $\Omega_2 e^{2iKy}$ and $\Omega_2^* e^{-2iKy}$.

Symmetries of the Hamiltonian H

For $\delta_R = 0$, the Hamiltonian H in Eq. (S13) is invariant under a generalized inversion symmetry, i.e., a spatial inversion ($y \rightarrow -y$) followed by the spin inversion ($|1\rangle, |2\rangle, |3\rangle, |4\rangle \rightarrow |4\rangle, |3\rangle, |2\rangle, |1\rangle$). The preservation of this generalized inversion symmetry guaranties that the energy spectrum $E(q_y)$ is symmetric with respect to q_y , i.e.,

$$E(q_y) = E(-q_y). \quad (\text{S22})$$

The Hamiltonian H is also invariant under a nonsymmorphic symmetry, which comprises a translational operation $\hat{G} = e^{-i\hat{p}d/(2\hbar)}$ ($d = 2\pi/\lambda$) followed by a unitary transformation \hat{U} given by

$$\hat{U} = \begin{pmatrix} 1 & 0 & 0 & 0 \\ 0 & -1 & 0 & 0 \\ 0 & 0 & -1 & 0 \\ 0 & 0 & 0 & 1 \end{pmatrix}. \quad (\text{S23})$$

That is, $\hat{U}\hat{G}H\hat{G}^{-1}\hat{U}^{-1} = H$. Defining the nonsymmorphic symmetry operator $\hat{S} = \hat{U}\hat{G}$, we readily obtain $[\hat{S}, H] = 0$, which implies that \hat{S} and H share the same set of eigenstates. The physical meanings of \hat{U} and \hat{G} are explained below. First, the translational operator \hat{G} can be understood as shifting the entire y coordinate to $y + d/2$ by half the lattice spacing. Applying \hat{G} to H , i.e. $\hat{G}H\hat{G}^{-1}$, the matrix elements $\langle 1|H|2\rangle$, $\langle 2|H|1\rangle$, $\langle 3|H|4\rangle$, and $\langle 4|H|3\rangle$ flip their sign. Second, the unitary transformation \hat{U} can be understood as flipping the sign of the second and third spin states. Applying \hat{U} to $\hat{G}H\hat{G}^{-1}$, i.e. $\hat{U}\hat{G}H\hat{G}^{-1}\hat{U}^{-1}$, the matrix elements $\langle 1|\hat{G}H\hat{G}^{-1}|2\rangle$, $\langle 2|\hat{G}H\hat{G}^{-1}|1\rangle$, $\langle 3|\hat{G}H\hat{G}^{-1}|4\rangle$, and $\langle 4|\hat{G}H\hat{G}^{-1}|3\rangle$ flip their sign. The Hamiltonian after these two symmetry operations (\hat{U} and \hat{G}) thus returns to the original Hamiltonian H .

$\hat{S}^2(= \hat{G}^2)$ is a translational operator corresponding to a shift of d in the y coordinate, such that $[\hat{S}^2, H] = 0$. Therefore, the Hamiltonian H is invariant after a shift of d in y , a discrete translational symmetry. The eigenvalues of H thus have a periodicity of d in y . The eigenwavefunctions of H can be written in the form of Bloch waves, $e^{iq_y y}w(y)$, where $w(y)$ has a period of d . Since the nonsymmorphic symmetry operator \hat{S} and the Hamiltonian H share the same set of eigenstates, we can construct the eigenwavefunctions of H (and \hat{S}) in the following two types (in the form of Bloch waves) by considering the physical meanings of \hat{S} mentioned

above:

$$\psi_p(q_y) = e^{iq_y y} (u_1(y) |1\rangle + u_2(y) |2\rangle + u_3(y) |3\rangle + u_4(y) |4\rangle) \quad (\text{S24})$$

$$\psi_m(q_y) = e^{iq_y y} (v_1(y) |1\rangle + v_2(y) |2\rangle + v_3(y) |3\rangle + v_4(y) |4\rangle), \quad (\text{S25})$$

where

$$\begin{aligned} u_1(y + d/2) - u_1(y) &= u_2(y + d/2) + u_2(y) = u_3(y + d/2) + u_3(y) \\ &= u_4(y + d/2) - u_4(y) = 0 \end{aligned} \quad (\text{S26})$$

$$\begin{aligned} v_1(y + d/2) + v_1(y) &= v_2(y + d/2) - v_2(y) = v_3(y + d/2) - v_3(y) \\ &= v_4(y + d/2) + v_4(y) = 0. \end{aligned} \quad (\text{S27})$$

Applying \hat{S} to Eqs. (S24, S25), one can verify that ψ_p and ψ_m are eigenfunctions of \hat{S} with the corresponding eigenvalues $\pm e^{iq_y d/2}$. With Eqs. (S26, S27), we can also see that $\psi_p(q_y)$ and $\psi_m(q_y)$ are still Bloch waves labeled by q_y .

Consider two sets of eigenfunctions $\{\psi_p(q_y), \psi_m(q_y)\}$ and $\{\psi_p(q_y + K), \psi_m(q_y + K)\}$. Their corresponding eigenvalues of the operator \hat{S} are $\{e^{iq_y d/2}, -e^{iq_y d/2}\}$ and $\{-e^{iq_y d/2}, e^{iq_y d/2}\}$. Thus, one obtains $\psi_p(q_y) = \psi_m(q_y + K)$ and $\psi_m(q_y) = \psi_p(q_y + K)$. This suggests two properties associated with the nonsymmorphic symmetry: (1) both $\psi_p(q_y)$ and $\psi_m(q_y)$ have a periodicity of $2K$ in q_y , and (2) $\psi_p(q_y)$ and $\psi_m(q_y)$ are offset from each other by K in q_y . Denote the corresponding eigenenergies (eigenvalues of H) for $\psi_p(q_y)$ and $\psi_m(q_y)$ as E_p and E_m , the energy spectrum also possesses properties associated with the nonsymmorphic symmetry and corresponding to (1) and (2) above. Corresponding to (1), we have

$$E_p(q_y) = E_m(q_y + K). \quad (\text{S28})$$

This suggests that the band structure has crossing points at some q_y . Recall that the Hamiltonian H with $\delta_R = 0$ possesses a generalized inversion symmetry in Eq. (S22). Provided the relations

in Eq. (S22) and Eq. (S28), we obtain

$$E_p(q_y) = E_m(-q_y + K). \quad (\text{S29})$$

Consequently, for $q_y = (2n + 1)K/2$ where n is an integer, E_p is equal to E_m , corresponding to a degenerate point (band crossing) in the band structure. Such a degeneracy at $q_y = (2n + 1)K/2$ is protected by the nonsymmorphic symmetry and the generalized inversion symmetry. If $\delta_R \neq 0$, the generalized inversion symmetry is broken while the nonsymmorphic symmetry is retained, the two branches still cross but at $q_y \neq (2n + 1)K/2$.

Furthermore, the two independent branches in the spin-mechanical momentum coupling scheme in Fig. 2A implies that the plane wave basis $\{|\hbar(q_y + nK); m\rangle\}$ in Eq. (S14) can also be decomposed into two subsets based on the nonsymmorphic symmetry. These two branches can be written in the following form:

$$\begin{aligned} \phi_p(q_y) = \sum_n & (c_{1,n} |q_y + 2nK; 1\rangle + c_{2,n} |q_y + 2nK + K; 2\rangle \\ & + c_{3,n} |q_y + 2nK + K; 3\rangle + c_{4,n} |q_y + 2nK; 4\rangle) \end{aligned} \quad (\text{S30})$$

and

$$\begin{aligned} \phi_m(q_y) = \sum_n & (d_{1,n} |q_y + 2nK + K; 1\rangle + c_{2,n} |q_y + 2nK; 2\rangle \\ & + d_{3,n} |q_y + 2nK; 3\rangle + d_{4,n} |q_y + 2nK + K; 4\rangle). \end{aligned} \quad (\text{S31})$$

Equating Eqs. (S30, S31) with Eqs. (S24, S25) respectively, the coefficients in the above equations satisfy

$$\begin{aligned} \sum_n c_{1,n} e^{i2nKy} &= u_1(y), & \sum_n c_{2,n} e^{i(2nK+K)y} &= u_2(y), \\ \sum_n c_{3,n} e^{i(2nK+K)y} &= u_3(y), & \sum_n c_{4,n} e^{i2nKy} &= u_4(y), \end{aligned} \quad (\text{S32})$$

and

$$\begin{aligned} \sum_n d_{1,n} e^{i(2nK+K)y} &= v_1(y), & \sum_n d_{2,n} e^{i2nKy} &= v_2(y), \\ \sum_n d_{3,n} e^{i2nKy} &= v_3(y), & \sum_n d_{4,n} e^{i(2nK+K)y} &= v_4(y). \end{aligned} \quad (\text{S33})$$

From Eqs. (S30, S31), we readily see that $\phi_p(q_y)$ and $\phi_m(q_y + K)$ are identical if one equates $d_{1,n}$ with $c_{1,n+1}$, $d_{4,n}$ with $c_{4,n+1}$, $d_{2,n}$ with $c_{2,n}$, and $d_{3,n}$ with $c_{3,n}$. Thus, Eqs. (S30, S31) respectively correspond to the band 1 and band 2 in the main text, providing another way to understand band crossings due to the nonsymmorphic symmetry.

Calculations of BEC wavefunctions in the real space

We solve the Hamiltonians H_{q_y} or H'_{q_y} to obtain the probability amplitude ($b_{n,m}^{q_y}$) of the constituent plane waves of the form, $b_{n,m}^{q_y} e^{i(q_y+nK)y} |m\rangle$, whose superposition gives the BEC wavefunction in the real space. From the BEC wavefunction, we obtain the variations of the density and phase in the real space for each spin state. For example, density and phase are illustrated in Fig. 1C and Fig. 3B for a BEC at $q_y = 0$ and $\delta_R = 0$ (both are used for all the calculations in this section) in the ground band in Fig. 2B and Fig. 3C, respectively. In addition to the results for the ground band, here we also perform calculations for a BEC in the first excited band in Fig. 2B and Fig. 3C.

Regarding Fig. 1C, we perform calculations using $\Omega = 2.3 E_r$, $\Omega_1 = 2.5 E_r$, $\Omega_2 = 3.4 E_r$, and $\varepsilon_0 = 2.4 E_r$, the same parameters as used in Fig. 2B. The calculated density and phase in the real space for each spin state are shown in Fig. S5A and Fig. S5B for a BEC in the ground and the first excited bands, respectively. The red line, green dashed line, blue circles and black squares respectively correspond to spin states $|1\rangle$, $|2\rangle$, $|3\rangle$, and $|4\rangle$.

The BEC wavefunction corresponding to Fig. S5A(B) can be described by $\phi_p(q_y = 0)$ ($\phi_m(q_y = 0)$) in Eq. (S30) (Eq. (S31)), an eigenfunction of the \hat{S} operator with an eigenvalue

of $e^{iq_y d/2} = 1$ ($-e^{iq_y d/2} = -1$). Due to the nonsymmorphic symmetry, we find that (1) The calculated density of each spin state has a periodicity of $d/2$. (2) For the ground band, the phase of spin states $|1\rangle$ and $|4\rangle$ ($|2\rangle$ and $|3\rangle$) have a period of $d/2$ (d). For the first excited band, the phase of spin states $|1\rangle$ and $|4\rangle$ ($|2\rangle$ and $|3\rangle$) have a period of d ($d/2$). In general, for $q_y \neq 0$, the phase of two spin states would have a periodicity of d while the phase of the other two would have a periodicity of $d/2$, because a nonzero q_y would only introduce an overall phase factor to the spin states at $q_y = 0$.

As discussed in the main text, an additional RF coupling between spin states $|1\rangle$ and $|2\rangle$, and $|3\rangle$ and $|4\rangle$ can break the nonsymmorphic symmetry. In this case, the calculated spin density and phase in the real space are shown in Fig. S6AB respectively for a BEC in the ground and the first excited bands in Fig. 3C. The periodicity of the density and phase for each spin state is identical to the periodicity of the Hamiltonian H' . The maximum density of the ground state sits at the center of each lattice site because of the s -wave nature of the ground state. The maximum density of the spin states $|1\rangle$ and $|4\rangle$ in first excited state no longer sits at the center of each lattice site. The locations of adjacent peak densities are separated by $d/2$.

Initial state preparations in experiments

We note that the eigenstate of the BEC at $q_y = 0$ in band 1 (band 2) shown in Fig. 2B has dominant populations in $|4\rangle$ and $|1\rangle$ ($|3\rangle$ and $|2\rangle$). Thus, to load the BEC into such an eigenstate, we first prepare a BEC at $|4\rangle$ ($|3\rangle$) at $\delta_R > 2.5 E_r$. For band 1, we then ramp on the Raman and microwave couplings Ω and $\Omega_{1,2}$ from zero to final values while ramping δ_R to zero in 15 ms. For band 2, we ramp on the microwave couplings $\Omega_{1,2}$ from zero to final values while ramping δ_R to $\sim 0.6 E_r$ in 15 ms. Subsequently, while keeping $\Omega_{1,2}$ at the final values, we ramp on the Raman coupling Ω from zero to final values in 5 ms during which we ramp δ_R to zero in 3 ms and then hold δ_R at zero for the rest 2 ms.

For the initial state preparation in the lowest band in Fig. 3B, we first prepare a BEC at $|4\rangle$ at $\delta_R > 5 E_r$. Then, we ramp on the Raman and microwave couplings Ω and $\Omega_{1,2}$ from zero to final values while ramping δ_R to zero in 15 ms. At the very beginning (at which $\delta_R > 5 E_r$, so the RF wave is off-resonant) of this 15-ms ramp, the RF coupling Ω_{RF} is abruptly turned on to the final value. Then, Ω_{RF} is held at the same final value while δ_R is ramped to zero in 15 ms.

For the initial state preparation at the minimum of the right well in Fig. 4B, we first prepare a BEC at $|4\rangle$ at $\delta_R > 2.5 E_r$. Then, we ramp on the Raman and microwave couplings Ω and Ω_1 from zero to final values while ramping δ_R to zero in 15 ms. In this case, Ω_2 is zero throughout the experiment.

Imaging analysis

The propagation direction (\hat{x}') of our imaging laser is $\sim 27^\circ$ with respect to the x -axis in the $x - z$ plane (Fig. 1A). Thus, the TOF images are in the $y - z'$ plane (where \hat{z}' is perpendicular to \hat{x}' in the $x - z$ plane). In each TOF image, we individually fit the atomic cloud of each spin and mechanical momentum component to a 2D bimodal distribution of the form:

$$A \max \left(1 - \left(\frac{y - y_c}{R_y} \right)^2 - \left(\frac{z' - z_c}{R_{z'}} \right)^2, 0 \right)^{3/2} + B \exp \left(-\frac{1}{2} \left(\left(\frac{y - y_c}{\sigma_y} \right)^2 + \left(\frac{z' - z_c}{\sigma_{z'}} \right)^2 \right) \right), \quad (\text{S34})$$

where the first term corresponds to the condensate part according to the Thomas-Fermi approximation and the second term corresponds to the thermal part. In our experiments, a nearly pure BEC with a typical condensate fraction $> 90\%$ is prepared at the end of the evaporation cooling. After turning on the couplings and loading the BEC into the band structure for initial state preparation before the transport measurement, the typical condensate fraction is $> 50\%$. After ~ 10 ms of transport in the band, the typical condensate fraction is $> 30\%$. The measured quantities presented in the main text, such as mechanical momentum and spin populations, are referred to the condensate part. For each atomic cloud component i , its condensate atom

number N_i and mechanical momentum p_i are extracted from the fitting to obtain the total mechanical momentum of the BEC, $\hbar k_{\text{BEC}} = N_i p_i / (\sum_i N_i)$. Each cloud component's mechanical momentum p_i is determined by the difference between its center-of-mass position (y_c) and the center-of-mass position of a BEC that has zero mechanical momentum, based on the calibrated conversion between $\hbar K$ and image pixels.

Calculated curves shown in the figures in the main text

When using the Hamiltonians H_{q_y} and H'_{q_y} (see Eq. (S15)) to calculate the band structures, we use n ranging from -13 to 13 , i.e., each Hamiltonian is a 108 by 108 matrix. On the other hand, H_{unzip} in Eq. (S21) is a 4 by 4 matrix. We solve the eigenstates of H_{q_y} , H'_{q_y} , and H_{unzip} , as a function of quasimomentum to obtain the corresponding mechanical momentum and spin compositions of the BEC traveling in bands. In general, the eigenstate is a normalized vector of the form $(\dots, b_{n,m}^{q_y}, \dots)^T$, where the coefficient $b_{n,m}^{q_y}$ is the probability amplitude ($|b_{n,m}^{q_y}|^2$ is the fractional population) corresponding to the state $|\hbar(q_y + nK); m\rangle$. The total mechanical momentum of the BEC at q_y is determined as $\hbar k_{\text{BEC}}(q_y) = \hbar \sum_{n,m} |b_{n,m}^{q_y}|^2 (q_y + nK)$. The fractional population of the spin state $|m\rangle$ at q_y is $\sum_n |b_{n,m}^{q_y}|^2$. The spin texture of band structures such as Fig. 2B is revealed by the q_y -dependent color, determined by the population-weighted colors of the constituent spin states. That is, the color of an eigenstate at q_y is determined by $\sum_m (\sum_n |b_{n,m}^{q_y}|^2) (\text{color})_m$, where $(\text{color})_m$ is a 1 by 3 vector representing the color of the spin state $|m\rangle$, with $(\text{color})_1 = (1, 0, 0)$ for red, $(\text{color})_2 = (0, 1, 0)$ for green, $(\text{color})_3 = (0, 0, 1)$ for blue, and $(\text{color})_4 = (0, 0, 0)$ for black. Note that the calculated $\hbar k_{\text{BEC}}$ versus quasimomentum is identical to the calculated $\frac{m}{\hbar} \frac{dE(q_y)}{dq_y}$ versus quasimomentum, because $\hbar k_{\text{BEC}}(q_y) = m v_p(q_y) = \frac{m}{\hbar} \frac{dE(q_y)}{dq_y}$, where E is the eigenenergy and $\frac{dE(q_y)}{dq_y}$ is the slope of the band.

The above calculated physical quantities are functions of q_y . They can be converted to functions of t_{hold} based on the measurement of quasimomentum versus t_{hold} in each set of ex-

periment. Fig. S7 is a representative measurement obtained from the experiment corresponding to Fig. 2C, showing the measured quasimomentum versus t_{hold} obtained from the atomic clouds of $|1\rangle$ and $|4\rangle$. The corresponding slope, $d(\hbar q_y)/d(t_{hold}) = F_g$, is the total force acting on the atoms during the transport and obtained by a linear fit to the data. The average of the slope, $0.751 \hbar K/ms$ in this case, is then used to calculate various physical quantities versus t_{hold} . Note this total force is primarily due to the gravity (which would give a slope of $0.843 \hbar K/ms$ with $g = 9.81 m/s^2$) but also contains a small contribution (with the opposite sign) from other background (e.g. magnetic) fields present during the experiment.

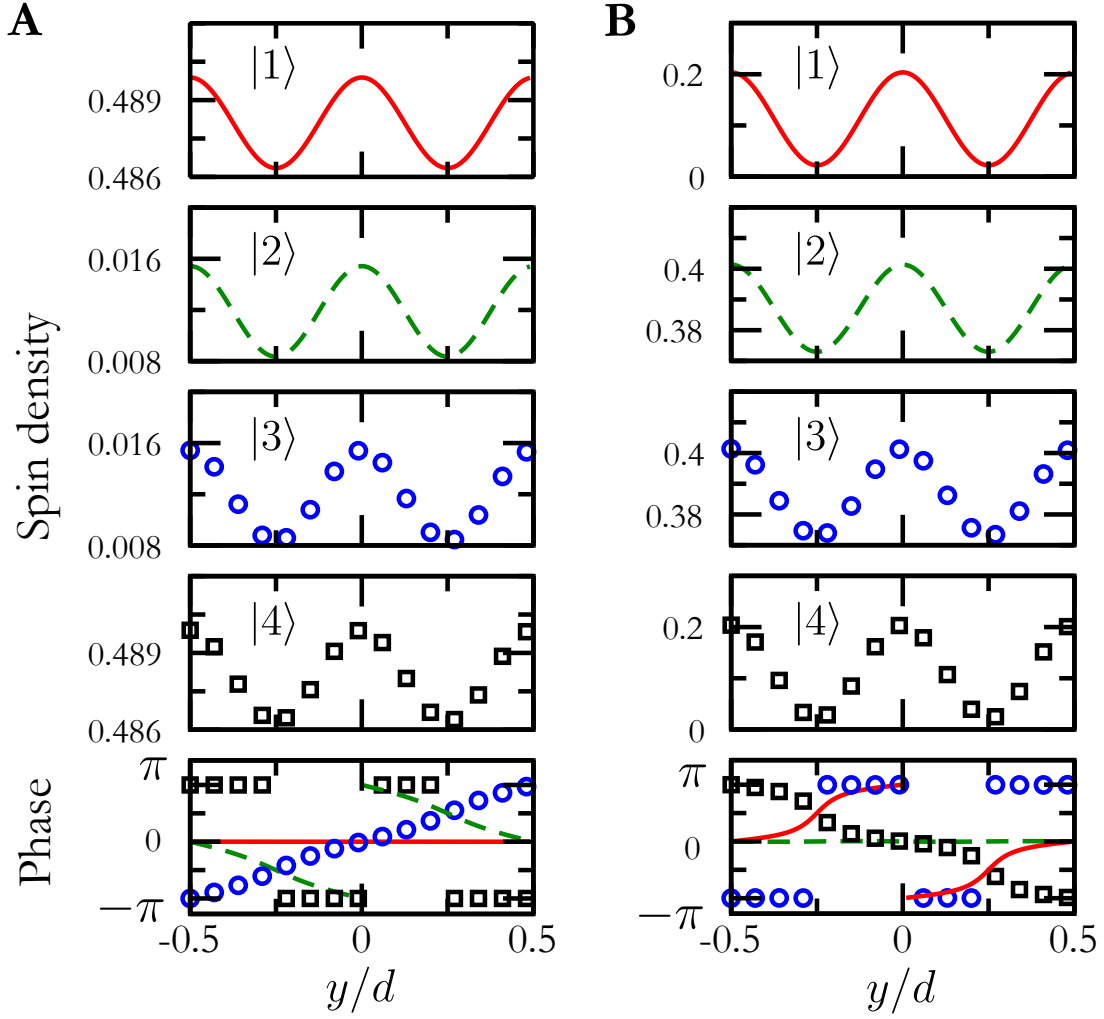


Figure S5: **Density and phase versus y for each spin state, corresponding to the Hamiltonian H .** Calculations are performed for a BEC at $q_y = 0$ in Fig. 2B, (A) for the ground band, and (B) for the first excited band. The red line, green dashed line, blue circles, and black squares correspond to the spin states $|1\rangle$, $|2\rangle$, $|3\rangle$, and $|4\rangle$, respectively.

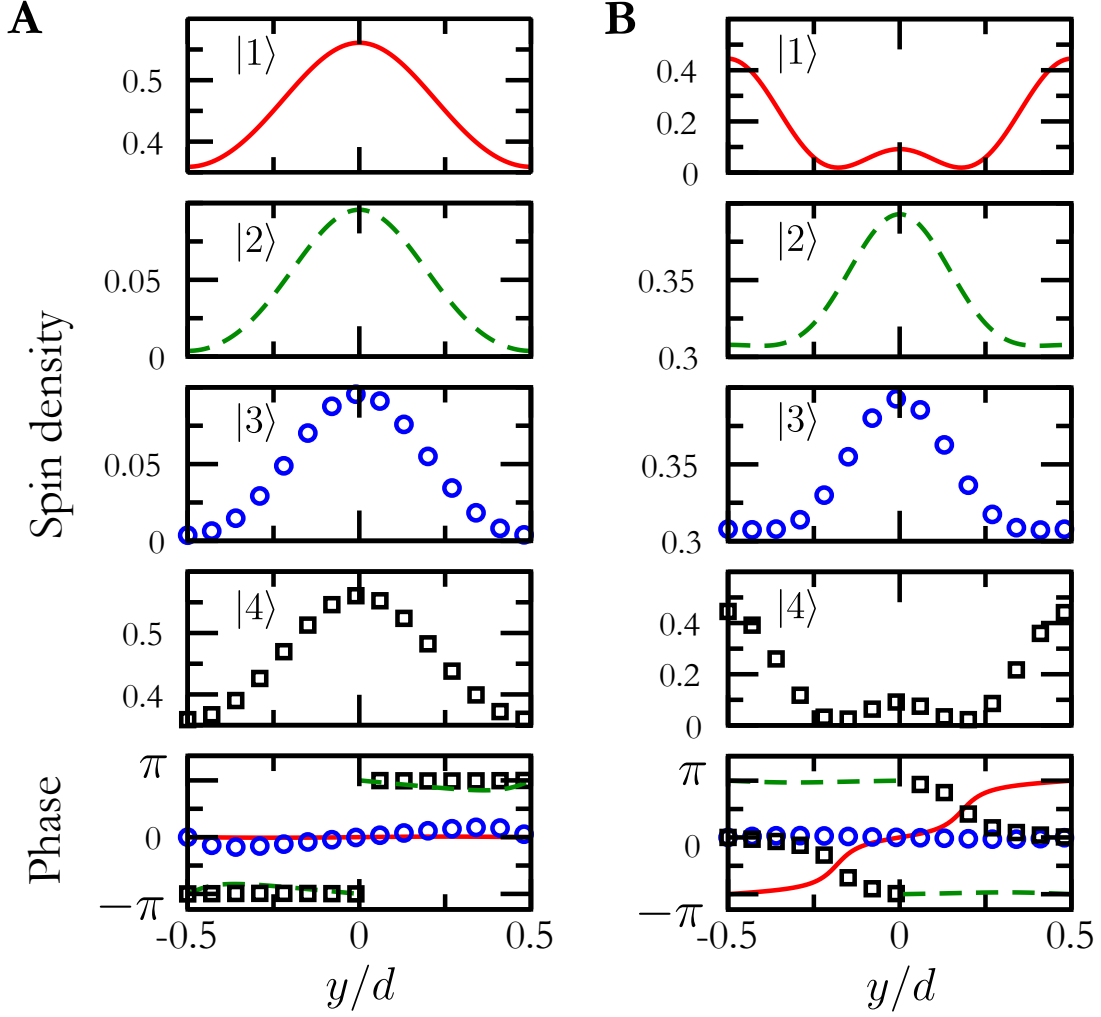


Figure S6: **Density and phase versus y for each spin state, corresponding to the Hamiltonian H' .** Calculations are performed for a BEC at $q_y = 0$ in Fig. 3C, (A) for the ground band, and (B) for the first excited band. The red line, green dashed line, blue circles, and black squares correspond to the spin states $|1\rangle$, $|2\rangle$, $|3\rangle$, and $|4\rangle$, respectively.

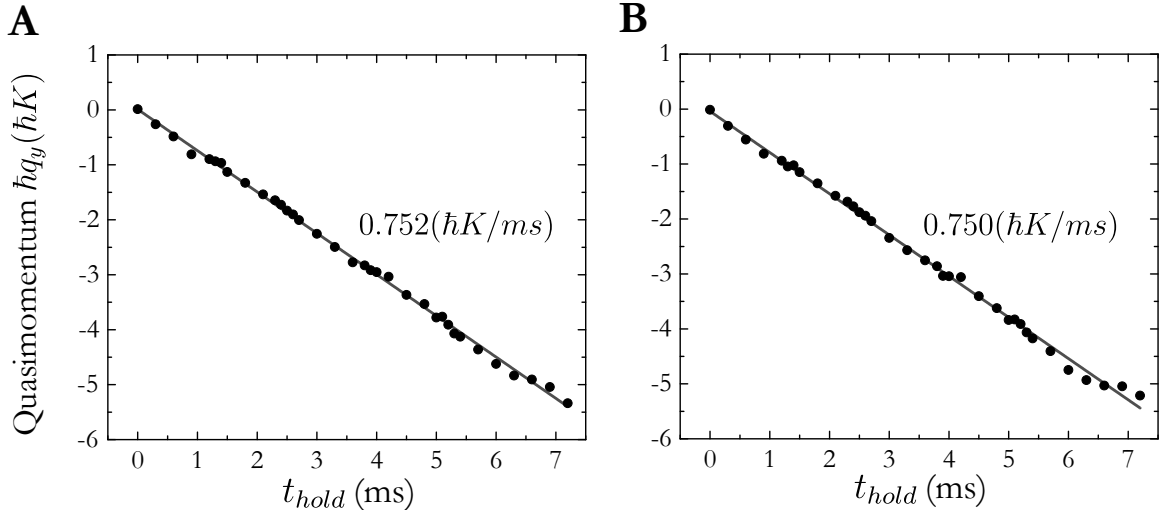


Figure S7: **Representative measurement of quasimomentum versus t_{hold} .** (A) and (B) are obtained respectively from the atomic clouds of $|1\rangle$ and $|4\rangle$ in the experiment corresponding to Fig. 2C. Dots are experimental data and lines are linear fits.